I. The training and testing process of the NEP model

The training datasets of the NEP potentials of Li_6NII_2 and Li_6NBrBr_2 consist of two parts, one is composed of the configurations sampled by PYNEP[1] from MD simulations at target temperatures and strains in the two-dimensional principal component descriptor space, as illustrated in Figure S2. The other is composed of manually added uniaxial strain, biaxial strain and rattled configurations, for Li_6NII_2 (Li_6NBrBr_2) are 20 (22).

Figure S5 displays the progressive development of each pertinent term contained in the loss function using the separable natural evolution strategy (SNES)[2] generation throughout the training procedure. As the number of generations increases, the root mean square error (RMSE) values of the energy, force, and virial converge, with only minimal changes in values at approximately 7×10^5 steps, thereby confirming the reliability and stability of the NEP models. Meanwhile, we conducted a comparison of the phonon dispersion results calculated using DFT and NEP, as illustrated in Figure S6. The findings indicate that the computational outcomes from both methods are largely consistent, thereby validating the high accuracy and strong generalization capability of the NEP model.

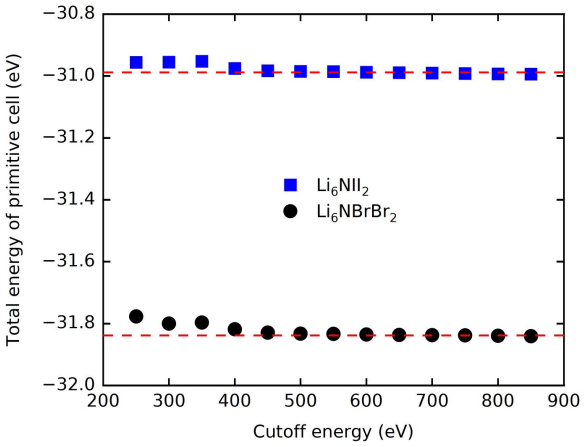

Figure S1. The variation trend of the total energy of the primitive cell with the cutoff energy.

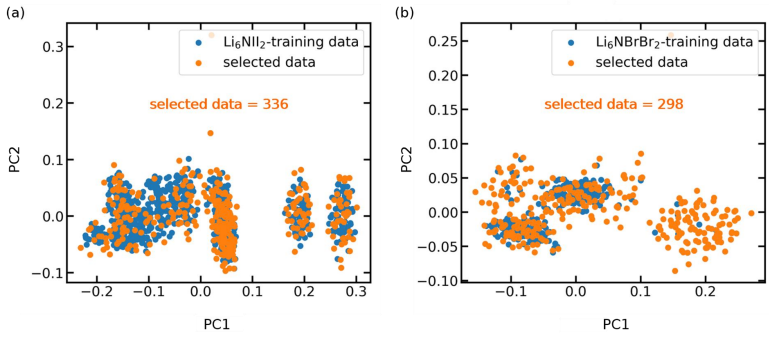

Figure S2. The distribution of the structures sampled by PYNEP of (a) Li_6NII_2 and (b) Li_6NBrBr_2 from the MD simulations under different temperatures and strains in the principal component 1 (PC1) and principal component 2 (PC2).

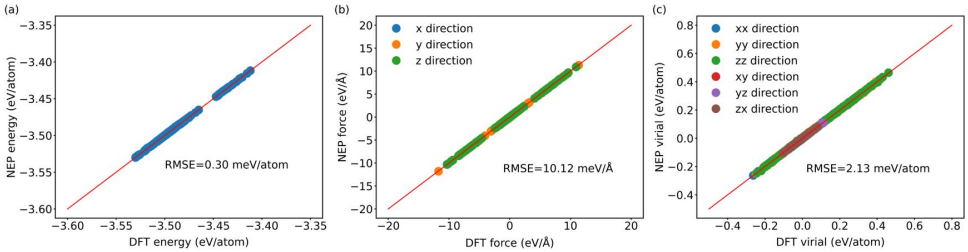

Figure S3. For Li_6NBrBr_2, (a) energy, (b) force, and (c) virial calculated by NEP compared to the relevant results calculated from DFT in the training dataset. The solid lines in (a) – (c) are the identity function applied to guide the eyes.

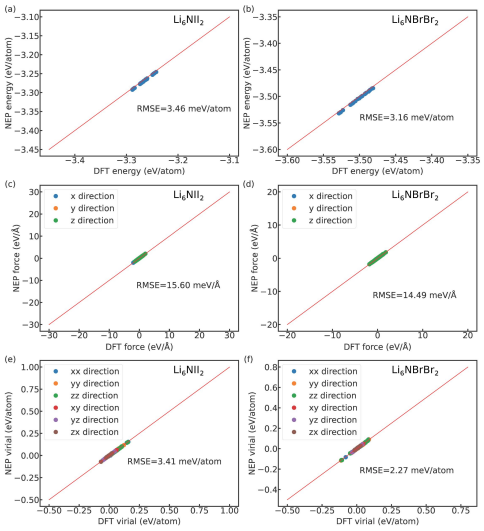

Figure S4. For Li_6NII_2 and Li_6NBrBr_2, (a)-(b) energy, (c)-(d) force and (e)-(f) virial calculated by NEP as compared to the relevant results calculated from DFT in the testing dataset. The solid lines in (a)-(e) are the identity function applied to guide the eyes.

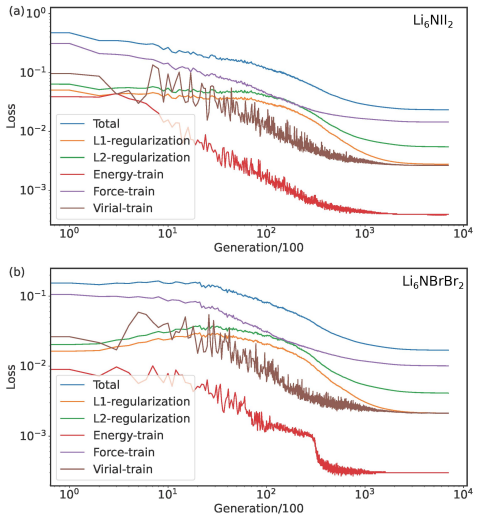

Figure S5. The evolving process of training loss terms for specific NEP models of (a) Li_6NII_2 and (b) Li_6NBrBr_2.

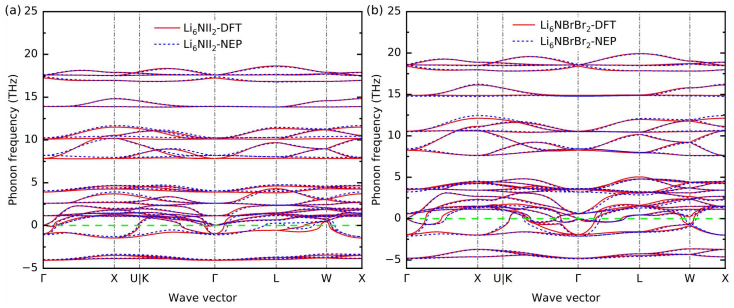

Figure S6. Phonon dispersion calculated by DFT and NEP for (a) Li_6NII_2 and (b) Li_6NBrBr_2 at 0 K.

II. Lattice structure information

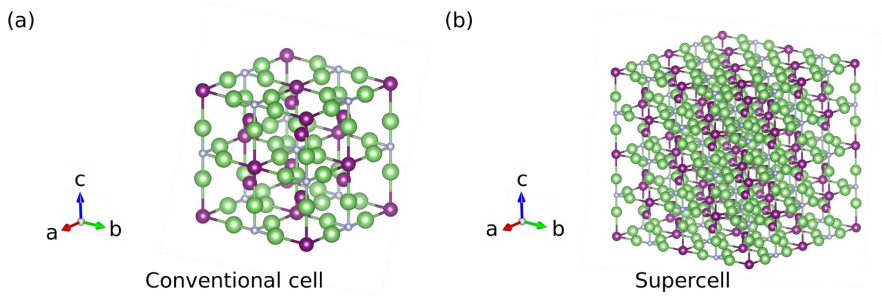

Figure S7. (a) The conventional cell (40 atoms) and (b) the supercell with 2 × 2 × 2 conventional cells (320 atoms) of Li_6NII_2 and Li_6NBrBr_2.

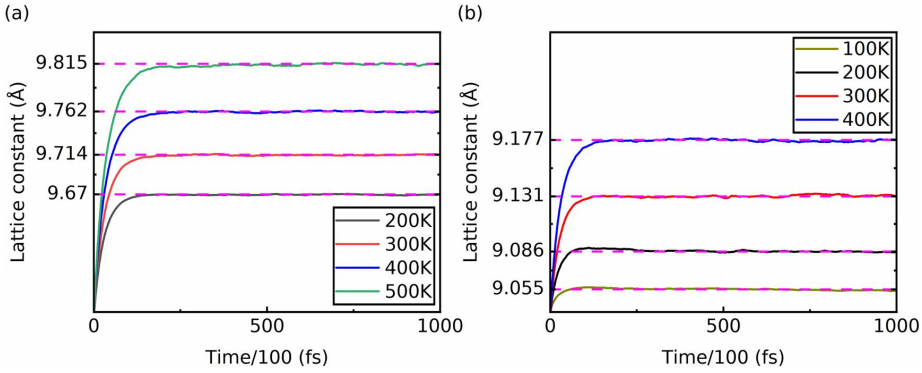

Figure S8. The temperature-dependent lattice constants as a function of simulation time of (a) Li_6NII_2 and (b) Li_6NBrBr_2 in MD simulations.

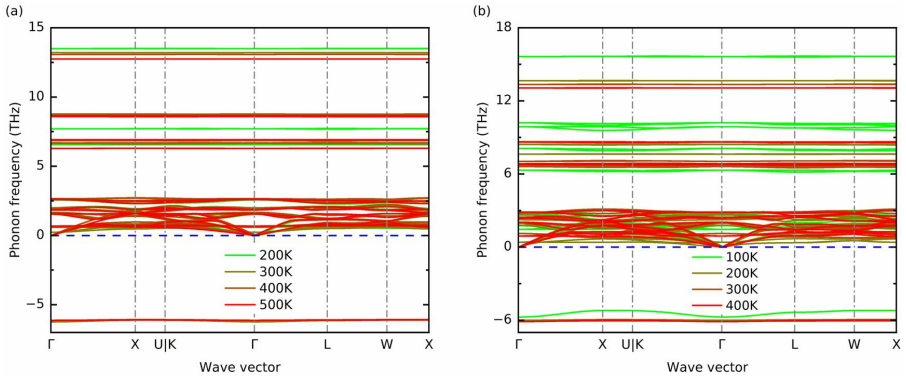

Figure S9. The temperature-dependent phonon dispersion relations of (a) Li_6NII_2 from 200 to 500 K and (b) Li_6NBrBr_2 from 100 to 400 K.

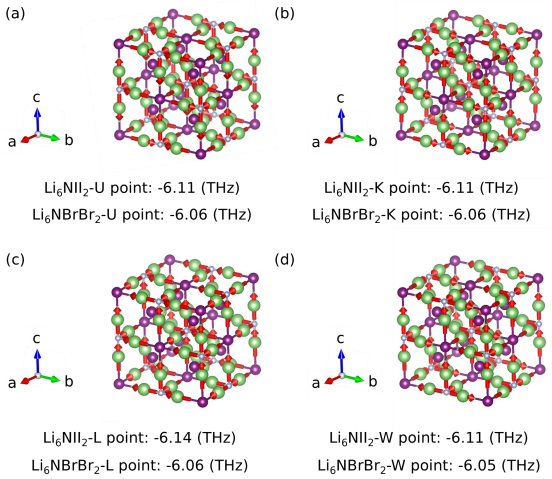

Figure S10. Phonon vibrational modes of Li_6NII_2 and Li_6NBrBr_2 at the (a) U, (b) K, (c) L and (d) W points at 300 K.

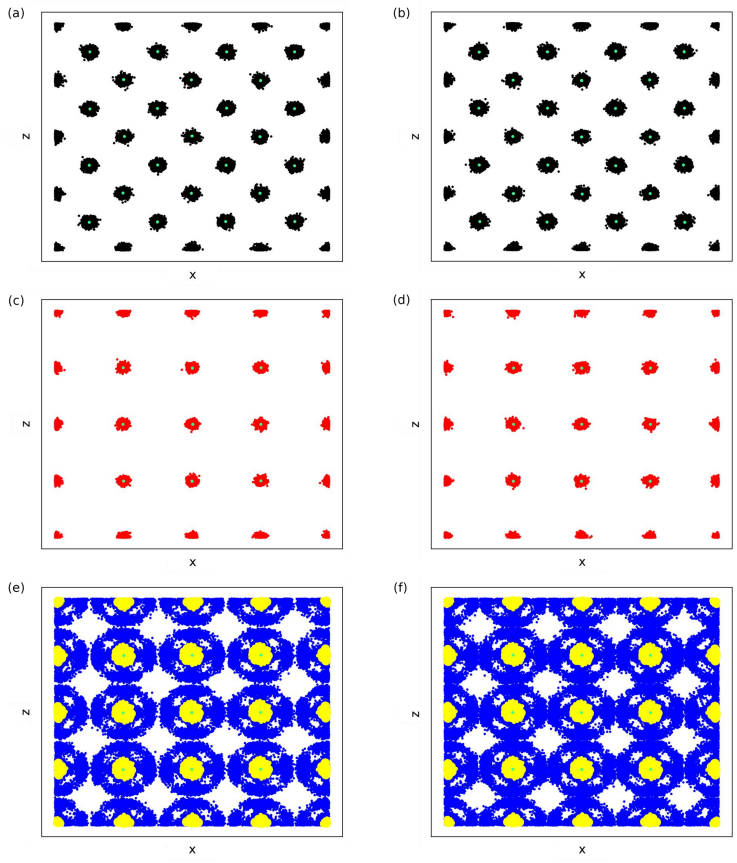

Figure S11. The projection on the xz plane of (a) I-ion, (b) Br-ion, (c-d) N-ion and (e-f) Li-ion, trajectories in Li_6NII_2 and Li_6NBrBr_2 supercell (2 × 2 × 2 conventional cells) at 300 K, respectively (blue: Li-ion hopping trajectories, yellow: Li-ion atomic vibration trajectories; red: N-ion atomic vibration trajectories; black: I/Br-ion atomic vibration trajectories; green: all-ion equilibrium positions).

III. The stability of Li_6NII_2 and Li_6NBrBr_2

The imaginary phonon bands, the eigenvectors of the phonon modes and the atomic contributions of nitrohalide double antiperovskites indicate that these imaginary phonon modes are only related to the Li-ion vibrations within a single conventional unit cell as shown in Figure 4(a), Figure 4(b) and Figure S10, which are due to the invalidation of perturbation theory. Therefore, the phonon dispersion relations alone cannot determine the stability of these materials, and it is challenging to obtain phonon group velocity and lifetimes using the phonon Boltzmann or Wigner transport equations.

Long-term *NPT* and *NVT* molecular dynamics simulations were conducted at target temperatures with first-principles accuracy. During simulations, lattice constant, temperature, energy, and pressure exhibit tiny and smooth fluctuations and convergence stably, as shown as Figure S12, Figure S13 and Figure S8. No crystal collapse, phase transformation or rotational distortion was found as shown in Figure 4(c), Figure S14, Figure S15 and Figure S11. Although there is no evidence of thermal stability in the synthesis experiments of the two materials, the above calculation results indicate that both materials are thermodynamically stable. There are other materials without stable phonon dispersions that can be thermodynamically stable, such as Li_2S[3], and high entropy alloys[4].

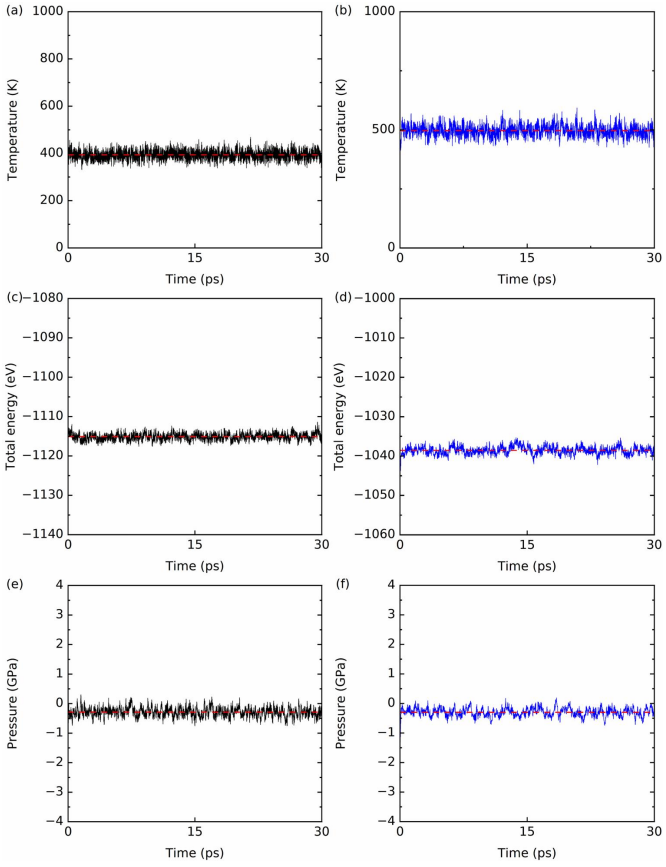

Figure S12. AIMD-NPT results for the (a-b) temperature, (c-d) energy, and (e-f) pressure of supercell (2 × 2 × 2 conventional cell), the black and blue lines represent the correlation results for Li_6NBrBr_2 and Li_6NII_2, respectively.

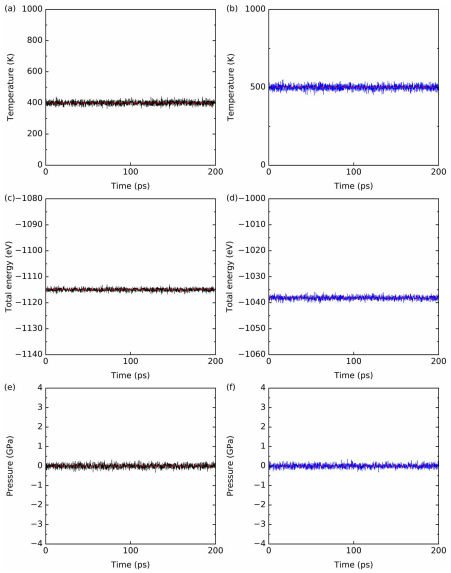

Figure S13. GPUMD-NPT results for the (a-b) temperature, (c-d) energy, and (e-f) pressure of supercell (2 × 2 × 2 conventional cell), the black and blue lines represent the correlation results for Li_6NBrBr_2 and Li_6NII_2, respectively.

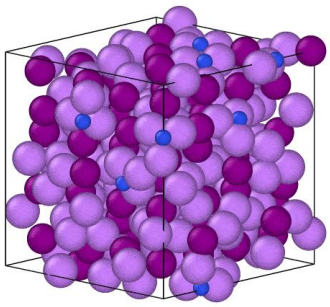

Figure S14. At 500 K, the structural changes of Li_6NII_2 supercell (2 × 2 × 2 conventional cell) in a 200 ps GPUMD-NPT simulation (lilac: Li ions, modena: I ions, blue: N ions).

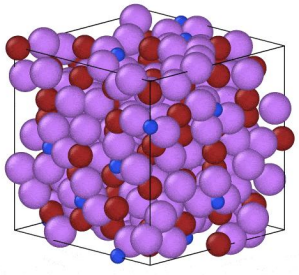

Figure S15. At 500 K, the structural changes of Li_6NII_2 supercell (2 × 2 × 2 conventional cell) in a 200 ps GPUMD-NPT simulation (lilac: Li ions, red: Br ions, blue: N ions).

IV. The convergence tests of thermal conductivity

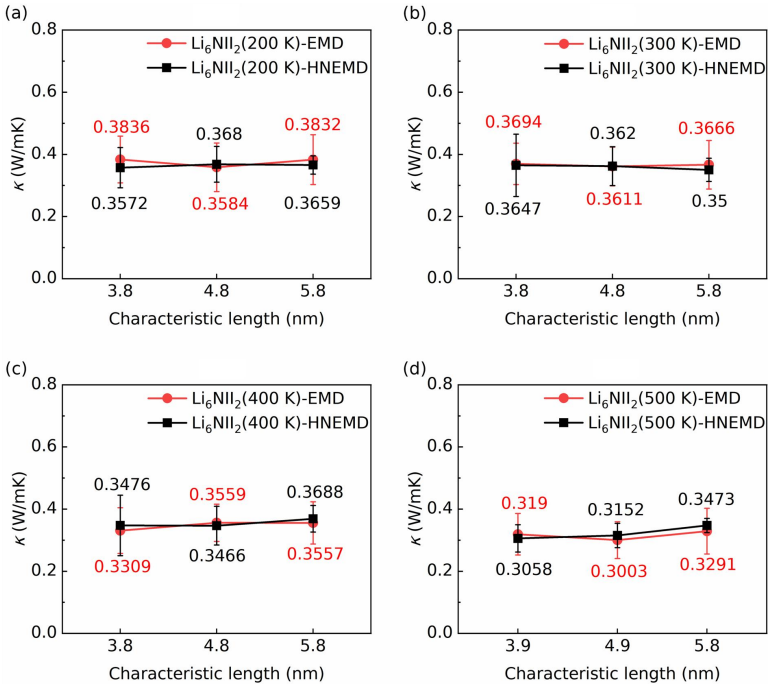

Figure S16. Lattice thermal conductivity κ as a function of the characteristic length for Li_6NII_2 at (a) 200 K, (b) 300 K, (c) 400 K and (d) 500 K from the HNEMD and EMD simulations.

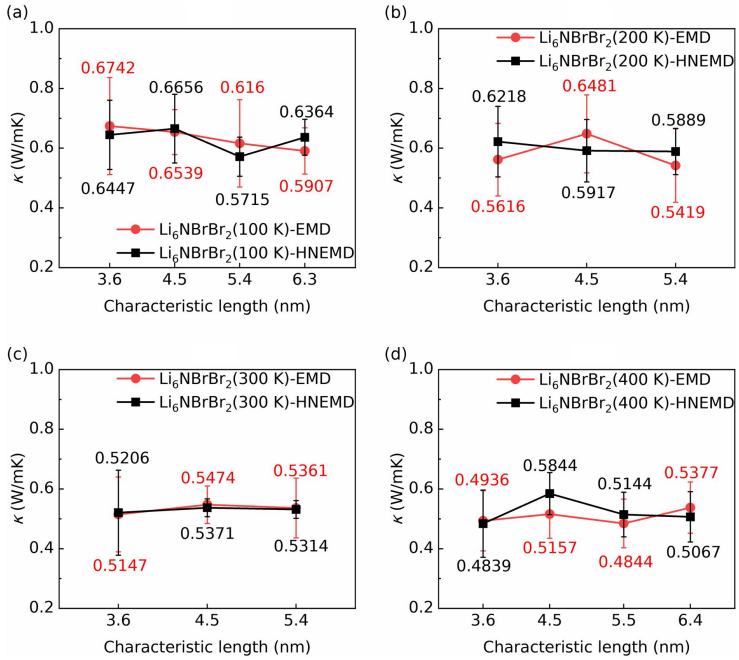

Figure S17. Lattice thermal conductivity κ as a function of the characteristic length for Li_6NBrBr_2 at (a) 100 K, (b) 200 K, (c) 300 K and (d) 400 K from the HNEMD and EMD simulations.

V. The thermal conductivity results calculated by EMD and HNEMD for both materials.

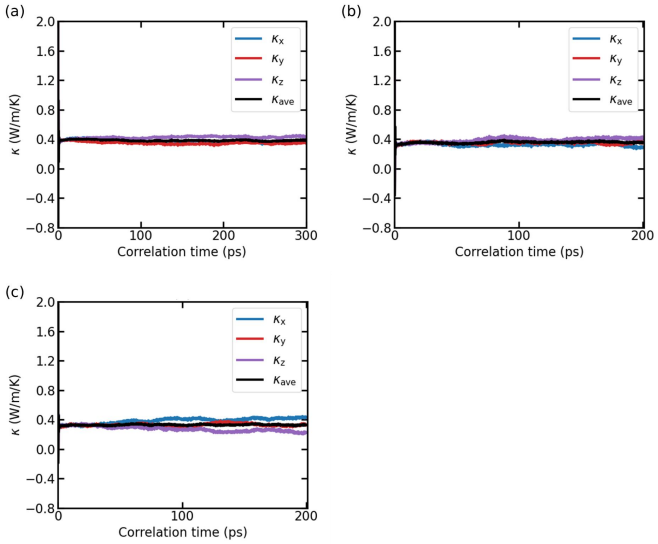

Figure S18. Running lattice thermal conductivity as a function of correlation time using the EMD method for Li_6NII_2 at (a) 200 K, (b) 400 K, (c) 500 K along the *x*, *y* and *z* directions, as well as their average. The sampling intervals for the heat current data are 20, 20, 4 and 2 fs from 200 to 500 K, respectively. 30 independent simulations were performed at 200, 400 and 500 K.

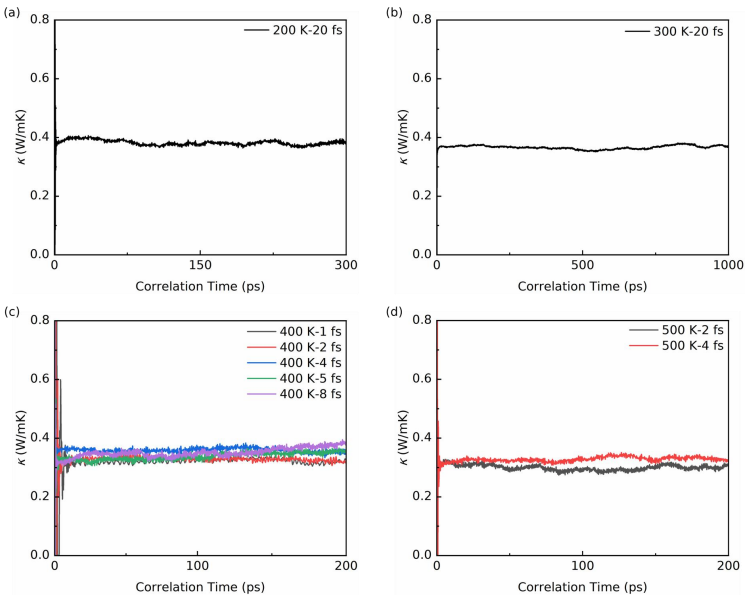

Figure S19. The variation of running thermal conductivity versus correlation time for different sampling interval values employed EMD for Li_6NII_2 from 200 to 500 K.

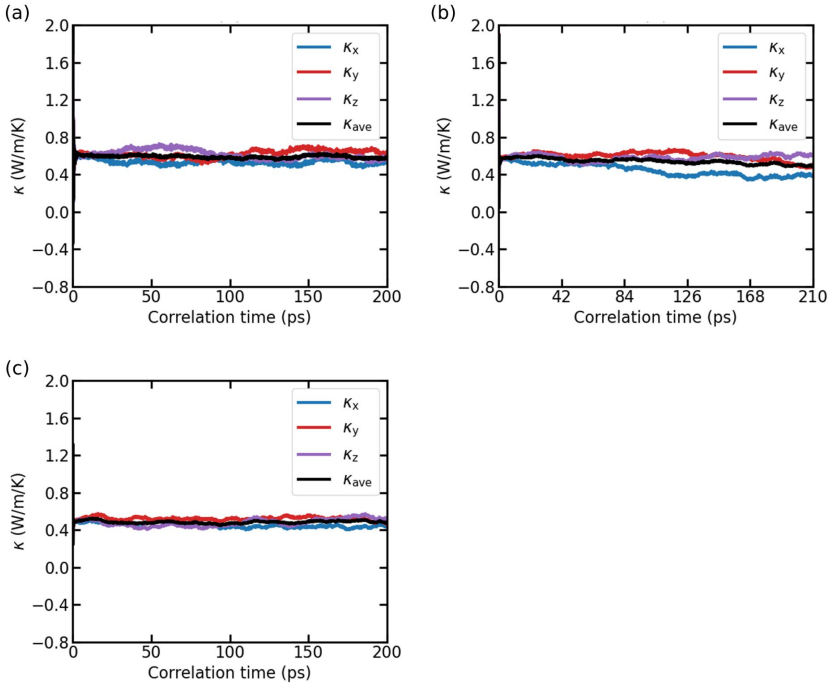

Figure S20. Running lattice thermal conductivity as a function of correlation time using the EMD method for Li_6NBrBr_2 at (a) 100 K, (b) 200 K, (c) 400 K along the *x*, *y* and *z* directions, respectively, as well as their average. The sampling intervals for the heat current data are 4, 6, 20 and 2 fs, respectively. 30 independent simulations were performed at 100, 200, 400 K.

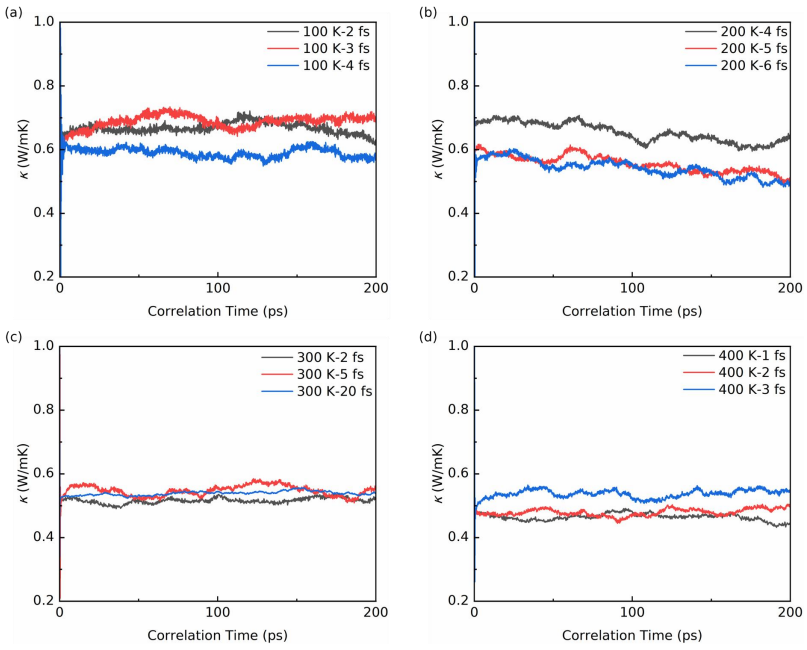

Figure S21. The variation of running thermal conductivity versus correlation time for different sampling interval values employed EMD for Li_6NBrBr_2 from 100 to 400 K.

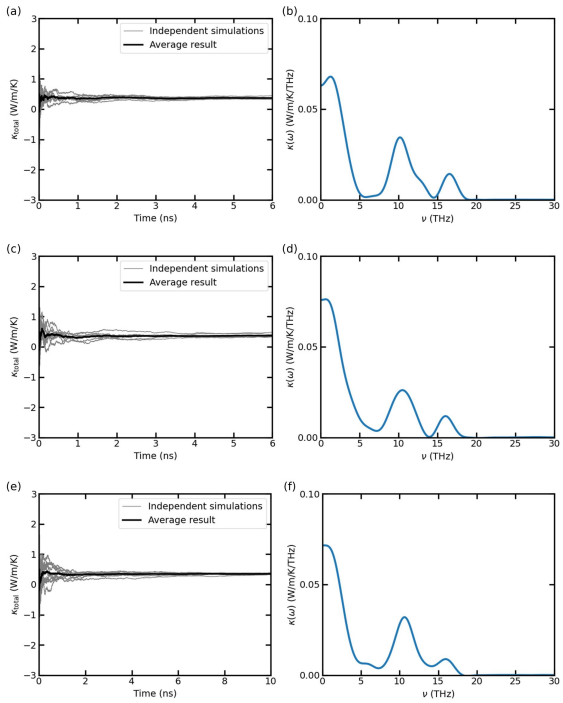

Figure S22. Running lattice thermal conductivity as a function of simulation time using the HNEMD method for Li_6NII_2 at (a) 200 K, (b) 400 K, (c) 500 K along the *y* direction and the corresponding spectral thermal conductivity (b), (d) and (f). Light grey lines represent 8 independent simulation times and their average result is colored by thick black. The driving forces are 2.3×10^{-4} Å^{-1}, 2×10^{-4} Å^{-1}, 1.8×10^{-4} Å^{-1} and 1.6×10^{-4} Å^{-1} from 200 to 500 K.

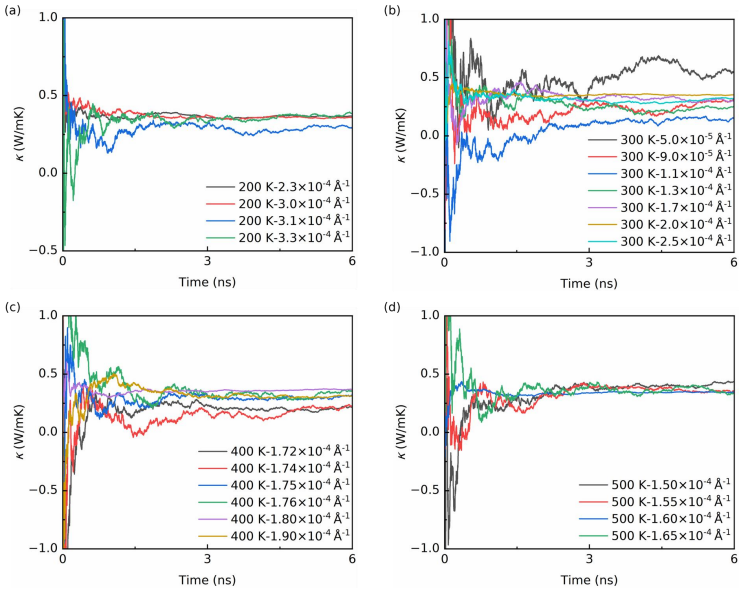

Figure S23. The variation of running thermal conductivity versus simulation time for different driving force values employed HNEMD for Li_6NII_2 from 200 to 500 K.

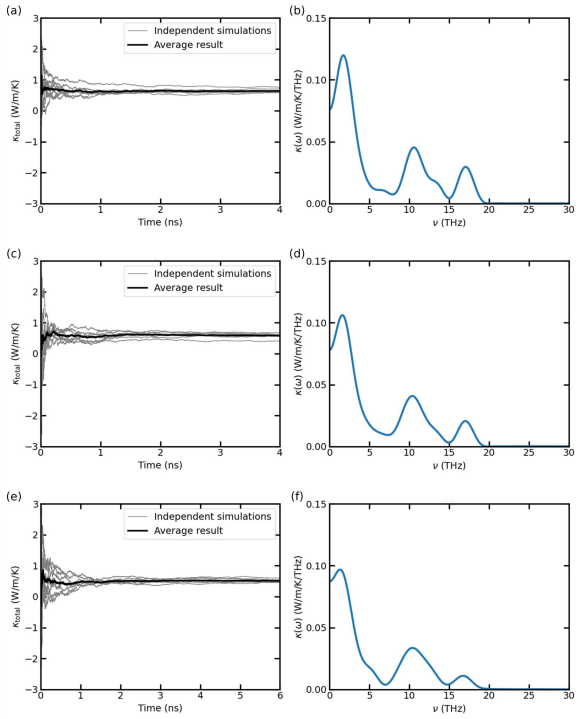

Figure S24. Running lattice thermal conductivity as a function of simulation time using the HNEMD method for Li_6NBrBr_2 at (a) 100 K, (b) 200 K, (c) 400 K along the y direction, respectively, and the corresponding spectral thermal conductivity (b), (d) and (f). Light grey lines represent 8 independent simulation times and their average result is colored by thick black. The driving forces are 2.5×10^{-4} Å^{-1}, 2.3×10^{-4} Å^{-1}, 2×10^{-4} Å^{-1} and 1.8×10^{-4} Å^{-1} from 100 to 400 K.

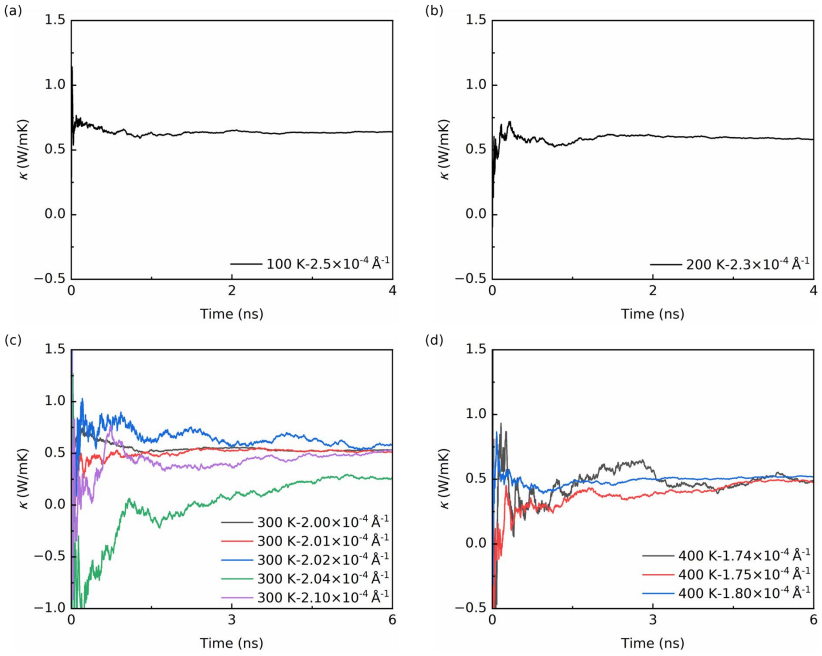

Figure S25. The variation of running thermal conductivity versus simulation time for different driving force values employed in the HNEMD method for Li_6NBrBr_2 from 100 to 400 K.

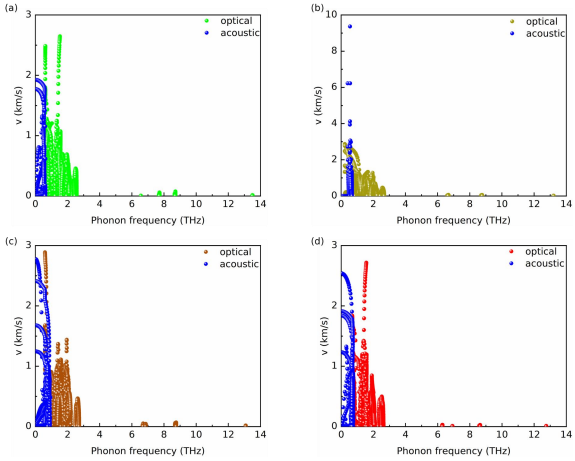

Figure S26. Mode-resolved group velocity vs phonon frequency in Li_6NII_2 at (a) 200 K, (b) 300 K, (c) 400 K and (d) 500 K.

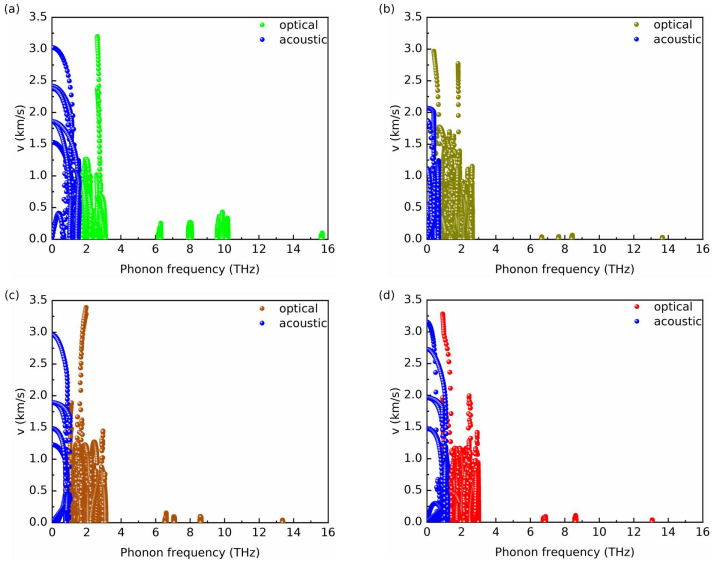

Figure S27. Mode-resolved group velocity vs phonon frequency in Li_6NBrBr_2 at (a) 100 K, (b) 200 K, (c) 300 K and (d) 400 K.

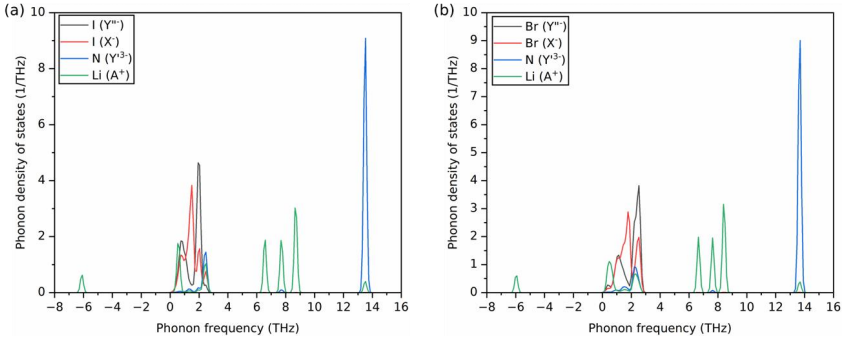

Figure S28. Phonon density of states of (a) Li_6NII_2 and (b) Li_6NBrBr_2 at 200 K.

VI. Settings of NEP hyperparameters

The hyperparameters include the radial and angular cutoff radii (r_c^R and r_c^A), the number of radial and angular descriptor components (n_{max}^R and n_{max}^A), the number of basis functions employed to construct the radial and angular descriptor functions (N_{bas}^R and N_{bas}^A), expansion order for angular terms encompassing three, four, and five-body terms (l_{max}^{3b}, l_{max}^{4b} and l_{max}^{5b}), the number of neurons in the hidden layer of the neural network (N_{neu}), the weight of two norm regularization terms in the loss function (λ_1 and λ_2), the weights of the loss term connected to the energy, forces and virial in the loss function (λ_e, λ_f and λ_v), the size of each batch used during the optimization procedure (N_{bat}), the number of generations for the SNES algorithm (N_{gen}) and the size of the population utilized by the SNES algorithm (N_{pop}).

Table S1. The hyperparameter settings of the NEP models of Li_6NII_2 and Li_6NBrBr_2.

Parameter	Li_6NII_2	Li_6NBrBr_2
NEP version	4	4
r_c^R r_c^A (Å)	7.7 5.9	7.2 5.5
n_{max}^R n_{max}^A	4 4	4 4
N_{bas}^R N_{bas}^A	12 12	12 12
l_{max}^{3b} l_{max}^{4b} l_{max}^{5b}	4 2 0	4 2 0
N_{neu}	30	30
λ_1 λ_2	-1 -1	-1 -1
λ_e λ_f λ_v	1.0 1.0 0.1	1.0 1.0 0.1
N_{bat}	1000	1000
N_{pop}	50	50
N_{gen}	700000	700000

Reference

1.Fan Z, Wang Y, Ying P, Song K, Wang J, Wang Y, et al. GPUMD: A package for constructing accurate machine-learned potentials and performing highly efficient atomistic simulations. J Chem Phys. 2022;157(11):114801. [DOI:10.1063/5.0106617]

2.Schaul T, Glasmachers T, Schmidhuber J. High dimensions and heavy tails for natural evolution strategies. In: Proceedings of the 13th annual conference on Genetic and evolutionary computation; 2011 July 12-16; Dublin, Ireland. New York: Association for Computing Machinery; 2011. p. 845-852.

3.Zhou Y, Xiong S, Zhang X, Volz S, Hu M. Thermal transport crossover from crystalline to partial-crystalline partial-liquid state. Nat Commun. 2018;9(1):4712. [DOI:10.1038/s41467-018-07027-x]

4.Samolyuk GD, Osetsky YN, Stocks GM, Morris JR. Role of static displacements in stabilizing body centered cubic high entropy alloys. Phys Rev Lett. 2021;126(2):025501. [DOI:10.1103/PhysRevLett.126.025501]